
Temporal Functional Circuits: From Spline Plots to Faithful Explanations in KAN Forecasting

Naveen Mysore

University of California, Santa Barbara

Dyssonance.ai

naveenmysore@ucsb.edu, nmysore.work@gmail.com

Abstract

Unlike MLPs, Kolmogorov-Arnold Networks (KANs) expose explicit learnable edge functions on every connection, enabling mechanistic explanation in time-series forecasting. This paper introduces *Temporal Functional Circuits*, a framework that transforms KAN edge functions from latent visualizations into faithful, temporally grounded explanations. Built on a *gated residual KAN* that decomposes forecasts into a linear base and a sparsely activated KAN correction, the framework (i) maps each edge to input lags via output-aware attribution, (ii) ranks edges by learned activation range, and (iii) validates faithfulness through edge-level interventions including zeroing and spline removal. Removing the learned B-spline component while retaining the base SiLU term degrades forecasts, providing evidence that the spline shape itself carries predictive value beyond the base activation. On four synthetic regimes of increasing complexity, the learned gate opens progressively wider as signal complexity grows. On regime-switching signals, gated KAN achieves 59% lower MSE than linear-only models. Across eight benchmarks, the gated architecture is competitive with linear, attention, and MLP alternatives, while providing interpretable edge functions that MLP-based corrections cannot offer.

1 Introduction

Long-term time-series forecasting (LTSF) is a core problem in climate science, energy management, transportation, and healthcare [Zhou et al., 2021, Wu et al., 2021]. Recent work has shown that simple linear models can match or outperform complex Transformer architectures on standard benchmarks [Zeng et al., 2023], raising the question of when additional model complexity is justified.

Kolmogorov-Arnold Networks (KANs) [Liu et al., 2025] provide an alternative to MLPs: instead of fixed activation functions on nodes, KANs place learnable univariate functions on edges, motivated by the Kolmogorov-Arnold representation theorem [Kolmogorov, 1957, Arnold, 1963]. These edge functions, typically parameterized as B-splines [de Boor, 1978], can be individually inspected, leading to claims that KANs are “inherently interpretable.” Several recent works apply KANs to time-series forecasting [Vaca-Rubio et al., 2024, Han et al., 2024, Huang et al., 2025], citing this interpretability as a key advantage.

A recent investigation of KAN-based forecasting is consistent with this complexity [Anonymous, 2026]. In controlled ablation experiments within a decomposition-patching pipeline, three forecasting cores (KAN, linear, attention) were compared across standard benchmarks (Table 4 in the appendix). The result showed that **no single core dominates**: KAN ranked first on Weather, linear on ETTh1, and results were near-tied on ETTm2. Each core ranked first on a different subset of datasets. This finding motivated the central question of this paper: *if KAN is not universally better, when does it help, and can we explain why?*

This paper argues that **visualizing learned splines is not the same as explaining forecasts**. A KAN edge function $\phi_e(z)$ operates in latent space: it does not directly indicate which input time steps or channels activated it, whether the model actually used it (versus suppressing it via downstream layers), or whether removing it would change the forecast. The saliency-map literature has shown that visually plausible explanations can fail basic sanity checks [Adebayo et al., 2018], and time-series models pose additional challenges because temporal autocorrelation can create superficially meaningful but unfaithful attribution patterns.

This work proposes a framework that transforms KAN edge functions from latent visualizations into *faithful, temporally grounded explanations*. The contributions are:

1. **Gated Residual KAN.** A forecasting architecture $\hat{y} = f_{\text{lin}}(x) + g(x) \odot f_{\text{KAN}}(x)$ with an L_1 -regularized gate $g(x) \in [0, 1]^C$ that provides a measurable KAN utilization metric U_{KAN} (averaged over channels and branches; formal definition in §3).
2. **Temporal Functional Circuits.** An explanation tuple $\mathcal{E}_e = (\phi_e, A_e, I_e, \Delta_e)$ per KAN edge, comprising the learned function, lag attribution, importance, and interventional effect (§4).
3. **Faithfulness validation.** Synthetic mechanism recovery on four regimes, edge deletion curves, and spline-removal interventions providing evidence that the B-spline component accounts for up to 41% of the full zeroing effect on Weather (§5).
4. **Empirical analysis.** Across eight benchmarks, the gated architecture is competitive with linear, KAN-only, attention, and MLP alternatives. Gate utilization correlates with an independent nonlinear residual diagnostic ($\rho = 0.46, p = 0.015$; §6).

2 Related Work

KANs and KAN-based time-series forecasting. KANs [Liu et al., 2025] place learnable univariate functions on edges rather than fixed activations on nodes, motivated by the Kolmogorov-Arnold representation theorem [Kolmogorov, 1957, Arnold, 1963]. Several works apply KANs to time-series forecasting: Vaca-Rubio et al. [2024] first demonstrate KANs as temporal approximators; KAN4TSF [Han et al., 2024] benchmarks KANs as MLP replacements; TimeKAN [Huang et al., 2025] integrates KANs with frequency decomposition; and KAN4TSF/RMoK [Han et al., 2024] uses mixture-of-KAN-expert routing. These works largely treat visualizable edge functions as interpretability evidence. This paper argues that time-series forecasting requires *temporal grounding* and *intervention-tested faithfulness*: the proposed gated residual design isolates nonlinear correction (unlike RMoK’s expert routing), and Temporal Functional Circuits map edges to raw lags, rank them by learned importance, and validate them through interventions.

Explainability for time series. Time-series XAI spans saliency-based methods [Ismail et al., 2020, Rojat et al., 2021, Theissler et al., 2022], learned perturbation masks [Crabbé and van der Schaar, 2021], windowed feature importance [Leung et al., 2023], and contrastive surrogate explanations [Queen et al., 2023]. Ismail et al. [2020] benchmark attribution methods on synthetic time series with known ground truth; this evaluation paradigm is adopted for the synthetic mechanism-recovery experiments. DynaMask [Crabbé and van der Schaar, 2021] learns dynamic masks over features and time steps, providing a baseline for the proposed edge-to-lag attribution. TimeX [Queen et al., 2023] trains an interpretable surrogate to explain black-box models. The present approach differs: rather than post-hoc surrogates, the model is explained through its *intrinsic* KAN edge functions, explicit univariate functions that can be inspected, edited, and intervened upon. Time-series shapelets [Ye and Keogh, 2009, Grabocka et al., 2014] offer another form of inherent interpretability via discriminative subsequences; the proposed temporal circuits are analogous but operate on learned edge functions grounded in forecast-horizon attribution rather than pattern matching.

Faithfulness and intervention-based evaluation. A central lesson from XAI research is that visual plausibility does not imply faithfulness [Adebayo et al., 2018, Jacovi and Goldberg, 2020]. Adebayo et al. [2018] showed that saliency maps can appear reasonable even for randomly parameterized models. The attention-as-explanation debate [Jain and Wallace, 2019, Wiegrefe and Pinter, 2019] further illustrates that inspectable internal objects (attention weights, or by analogy KAN splines) are not automatically faithful. Rudin [2019] argues for intrinsically interpretable models; KANs partially satisfy this via explicit edge functions, but this work shows that faithfulness still requires intervention testing. The evaluation draws on attribution axioms from Integrated Gradients [Sundararajan et al.,

2017], concept-level testing from TCAV [Kim et al., 2018], and the mechanistic-interpretability tradition of activation patching and circuit analysis [Olah et al., 2020, Geiger et al., 2021]. These ideas are adapted to the time-series KAN setting: edge removal and spline-removal interventions establish *model-internal* interventional effects, without claiming real-world causality in the data-generating process.

Forecasting backbones and gating. The controlled comparison builds on DLinear [Zeng et al., 2023], PatchTST [Nie et al., 2023], iTransformer [Liu et al., 2024], and RevIN [Kim et al., 2022]. The gated architecture relates to MoE designs [Jacobs et al., 1991, Shazeer et al., 2017], TFT’s gates [Lim et al., 2021], and MoLE [Ni et al., 2024]. Recent KAN-specific gating [Inzirillo and Genet, 2024b,a, Kim et al., 2025, Hasan et al., 2026] uses gating for *performance routing*; our gate instead serves a dual purpose: suppressing KAN when unnecessary *and* providing a measurable diagnostic (U_{KAN}). For edge importance, the original KAN [Liu et al., 2025] uses data-dependent L_1 pruning; CausalKANs [Almodóvar et al., 2025] and QuantKAN [Fuad and Chen, 2025] extend this to causal and quantized settings. The proposed R_e instead uses data-independent activation range over the B-spline grid.

3 Gated Residual KAN

Given an input window $x \in \mathbb{R}^{L \times C}$ of L time steps across C variates, the forecast $\hat{y} \in \mathbb{R}^{H \times C}$ is computed via:

$$\hat{y} = f_{\text{lin}}(x) + g_{\text{trend}}(x) \odot f_{\text{KAN}}^{\text{trend}}(x) + g_{\text{resid}}(x) \odot f_{\text{KAN}}^{\text{resid}}(x), \quad (1)$$

where f_{lin} is a linear forecasting branch, $f_{\text{KAN}}^{\text{trend}}$ and $f_{\text{KAN}}^{\text{resid}}$ are KAN-based nonlinear branches applied to trend and residual components respectively, and $g_{\text{trend}}, g_{\text{resid}} \in [0, 1]^C$ are per-channel scalar gates.

Pipeline. Both branches share a common preprocessing pipeline. **(1) RevIN** [Kim et al., 2022] normalizes each window to zero mean and unit variance per channel, storing statistics for denormalization. **(2) Adaptive normalization** encodes the temporal shape of the RevIN-normalized input via a two-layer MLP into a compact statistics vector $s \in \mathbb{R}^{d_s}$ ($d_s=8$), then produces a learned per-channel scale and shift: $x' = \gamma(s) \cdot x + \beta(s)$, where $(\gamma, \beta) = \text{Linear}(s)$ initialized to identity. **(3) Decomposition** splits the signal into trend and residual components via a moving-average filter [Wu et al., 2021]. Each component is processed independently with its own gate (Equation 1). The linear branch combines both: $f_{\text{lin}} = f_{\text{lin}}^{\text{trend}} + f_{\text{lin}}^{\text{resid}}$. All processing is channel-independent: x is reshaped from $[B, L, C]$ to $[B \cdot C, L]$ before entering the branches.

Linear branch. The input is divided into overlapping patches of length P with stride S , embedded via a linear layer into dimension d , flattened, and projected to the forecast horizon H through a single linear head. Under the shared preprocessing pipeline, this branch captures temporal patterns expressible as a linear function of patch embeddings.

KAN branch. The same patching produces token embeddings that are flattened and processed through a B-spline KAN [Liu et al., 2025, Blealtan, 2024] with two hidden layers. Each KAN edge implements a learnable univariate function $\phi_e(z) = w \cdot \text{SiLU}(z) + \sum_k c_k B_k^p(z)$, where B_k^p are cubic B-spline basis functions. This branch captures nonlinear residual structure that the linear branch cannot.

Gate. The gate network maps the flattened input to a single scalar per channel via a two-layer MLP with sigmoid activation: $g_c(x) = \sigma(\text{MLP}(x_c)) \in [0, 1]$. The gate value is broadcast across all forecast horizons.

Training objective.

$$\mathcal{L} = \text{MSE}(\hat{y}, y) + \lambda_g (\mathbb{E}[\|g_{\text{trend}}(x)\|_1] + \mathbb{E}[\|g_{\text{resid}}(x)\|_1]), \quad (2)$$

where λ_g controls gate sparsity. The L_1 penalty encourages both gates to remain closed (use linear only) unless the KAN correction genuinely reduces forecast error.

Circuit Walkthrough: Tracing a Weather Forecast Through a Temporal Functional Circuit

Edge e : input dim 1299 \rightarrow hidden 17 | Patch [320, 336] | $R_e = 0.74$ | Gate $g = 0.034$

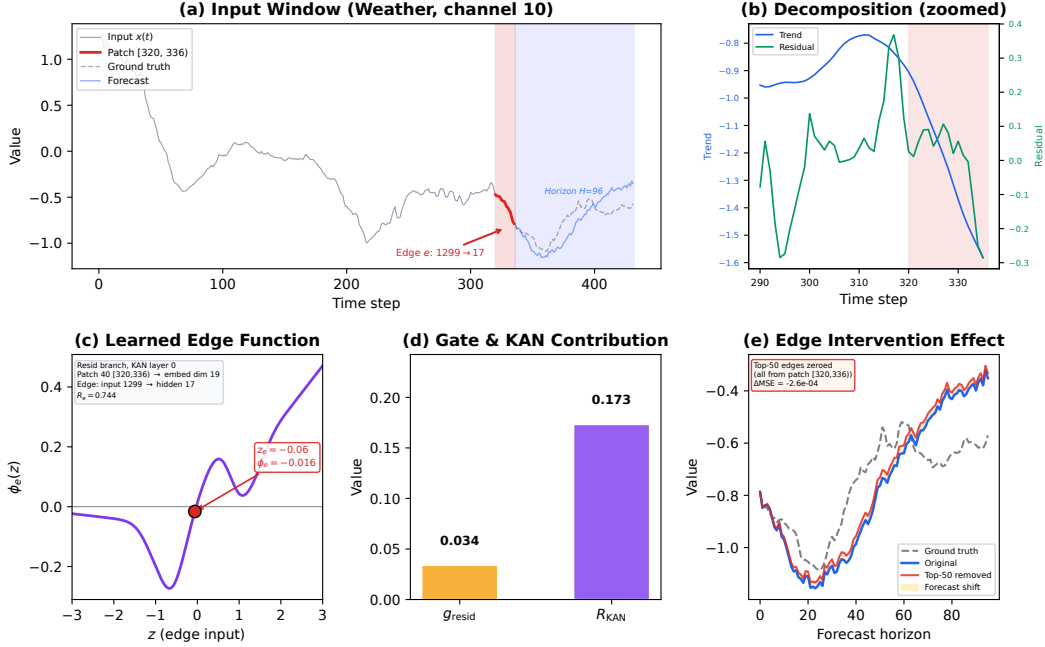


Figure 1: Circuit walkthrough on Weather (channel 10). (a) Input window with the top-attributed patch [320, 336] highlighted. (b) Trend/residual decomposition at the patch region (dual axes; residual is small). (c) Learned B-spline edge function $\phi_e(z)$ for the top edge by R_e , with the actual data point marked. (d) Gate value and calibrated KAN contribution R_{KAN} for this window. (e) Forecast with and without the top-50 edges by R_e : removing them visibly shifts the prediction, providing evidence that these edges carry functional load.

KAN utilization. Since the architecture has separate gates for trend and residual branches, we define $U_{KAN} = \frac{1}{2C} \sum_{c=1}^C (\mathbb{E}[g_{\text{trend},c}(x)] + \mathbb{E}[g_{\text{resid},c}(x)])$ as a scalar summary (averaged over channels C) of how much each dataset relies on nonlinear correction. A dataset with $U_{KAN} \approx 0$ is well-served by linear forecasting; $U_{KAN} > 0$ suggests the trained model uses nonlinear KAN correction under the chosen gate penalty.

4 Temporal Functional Circuits

A KAN edge function $\phi_e(z)$ operates in latent space; it does not directly reveal which input lags drove it, whether the model actually used it, or whether removing it changes the forecast. A *Temporal Functional Circuit* is defined as a tuple $\mathcal{E}_e = (\phi_e, A_e, I_e, \Delta_e)$ that answers each of these questions. Figure 1 illustrates a complete circuit walkthrough on a Weather test window: from the input signal through decomposition, to the learned edge function and its interventional effect on the forecast.

4.1 Edge-to-Lag Attribution

Each KAN edge e in the first layer maps from patched input dimension i to hidden dimension j . Through the patch embedding geometry, dimension i corresponds to patch index $p = \lfloor i/d \rfloor$, providing a coarse receptive field over raw lags $[p \cdot S, p \cdot S + P)$. Because the patch embedding mixes all P lag values through a learned linear projection, exact lag attribution requires gradients through the embedding. The output-aware edge contribution:

$$C_e(x) = \phi_e(z_e(x)) \cdot \frac{\partial \hat{y}}{\partial a_e}, \quad (3)$$

where $a_e = \phi_e(z_e)$ is the scalar edge activation and $\partial \hat{y} / \partial a_e$ captures downstream sensitivity (summed over output channels and horizons for scalarization, with stop-gradient to avoid second-order deriva-

tives). Because \hat{y} depends on $g(x) \odot f_{\text{KAN}}(x)$ (Equation 1), the gate is implicitly incorporated in $\partial\hat{y}/\partial a_e$ via the chain rule; when the gate is closed, the gradient is near zero regardless of edge activation. The temporal attribution is:

$$A_e(c, t) = \mathbb{E}_{x \sim \mathcal{D}} \left[\left| \frac{\partial C_e(x)}{\partial x_{c,t}} \right| \right]. \quad (4)$$

Because the model is channel-independent (x is reshaped to $[B \cdot C, L]$), c indexes the channel *being processed*, not cross-channel influence. $A_e(c, t)$ tells us which time steps within each channel the edge responds to.

4.2 Data-Weighted Edge Importance

Edges are ranked by their expected contribution to the forecast:

$$I_e = \mathbb{E}_{x \sim \mathcal{D}} \left[\left| \phi_e(z_e(x)) \cdot \frac{\partial \hat{y}}{\partial a_e} \right| \right]. \quad (5)$$

This combines two observable factors: (1) edge output magnitude—does the edge fire on real data? and (2) downstream sensitivity—does the edge affect the forecast? The gate’s influence enters implicitly through the gradient: $\partial\hat{y}/\partial a_e = g(x) \cdot \partial f_{\text{KAN}}/\partial a_e \cdot (\partial\hat{y}/\partial f_{\text{KAN}})$, so edges in a closed-gate branch automatically receive near-zero importance. Edges with large I_e are the functionally important components of the nonlinear correction.

A simpler alternative ranks edges by their activation range $R_e = \max_{z \in [t_0, t_G]} \phi_e(z) - \min_{z \in [t_0, t_G]} \phi_e(z)$, evaluated over the B-spline grid interval $[t_0, t_G]$ (the learned knot boundaries), which measures functional capacity without requiring data. Direct comparison shows R_e produces $20\times$ larger deletion effects than I_e on Weather (Appendix H), suggesting that for B-spline KANs, learned functional capacity is itself a strong faithfulness signal. R_e is therefore used as the primary ranking in deletion experiments.

4.3 Edge Interventions

To validate faithfulness, the *interventional effect* of editing edge e on predictive loss:

$$\Delta_e = \mathbb{E}_{(x,y) \sim \mathcal{D}_{\text{test}}} \left[\ell(f^{(-e)}(x), y) - \ell(f(x), y) \right], \quad (6)$$

where $f^{(-e)}$ denotes the model with edge e intervened upon. Positive Δ_e means the edge is beneficial. Three intervention types are considered:

- **Zero:** $a_e(x) \leftarrow 0$ (silence the edge completely).
- **Mean:** $a_e(x) \leftarrow \mathbb{E}[a_e]$ (replace with population mean, avoiding out-of-distribution internal states).
- **Spline removal:** remove only the B-spline component, retaining $\phi_e(z) = w \cdot \text{SiLU}(z)$ (tests whether the learned spline shape matters beyond the base activation; this is KAN-specific).

Note: Δ_e measures the edge’s interventional effect on the *model’s computation*, not a causal claim about the data-generating process.

Deletion curves. For aggregate faithfulness, all edges are ranked by an importance proxy (computed on validation data) and progressively delete the top- k , random- k , or bottom- k edges, measuring MSE increase on the *test set*. A faithful ranking satisfies: $\Delta_{\text{top-}k} > \Delta_{\text{random-}k} > \Delta_{\text{bottom-}k}$.

5 Experiments

5.1 Setup

Datasets. The evaluation covers eight benchmarks: seven standard LTSF datasets (Weather, 21 variates; Solar, 137; ECL, 321; ETTh1, ETTh2, ETTm1, ETTm2, 7 each) plus PPG-DaLiA [Reiss et al., 2019] (12 variates, physiological signals). All datasets use chronological train/validation/test splits following established LTSF protocols. ECL is included in the core ablation (Table 1) but excluded from multi-horizon and diagnostic analyses due to its high computational cost (321 variates \times 4 horizons \times 3 seeds); all reported correlations use $n = 28$ (7 datasets \times 4 horizons).

Table 1: Core ablation at $H = 96$ (MSE, mean \pm std over 3 seeds). Bold: best unrounded mean per dataset; rounded ties may appear identical. All cores use identical preprocessing.

Core	Weather	ETTh1	ETTh2	ETTh1	ETTh2	Solar	ECL	PPG
Linear	.152 \pm .001	.453 \pm .010	.240 \pm .002	.350 \pm .002	.150 \pm .002	.204 \pm .001	.131 \pm .000	.564 \pm .001
KAN	.149 \pm .001	.477 \pm .022	.244 \pm .000	.348 \pm .000	.150 \pm .001	.183 \pm .000	.132 \pm .000	.559 \pm .001
Attention	.150 \pm .002	.460 \pm .012	.251 \pm .003	.347 \pm .002	.150 \pm .001	.180	.129 \pm .000	.564 \pm .002
Ungated	.150 \pm .001	.451 \pm .006	.245 \pm .003	.347 \pm .002	.149 \pm .001	.180 \pm .001	.132 \pm .000	.563 \pm .002
Gated KAN	.149 \pm .001	.451 \pm .007	.243 \pm .003	.345 \pm .003	.148 \pm .001	.182 \pm .000	.132 \pm .001	.564 \pm .001
Gated MLP	.150 \pm .001	.453 \pm .008	.239 \pm .003	.347 \pm .003	.149 \pm .001	.185 \pm .001	.131 \pm .000	.563 \pm .001

Solar uses $\lambda_g = 0.01$; all others $\lambda_g = 0.05$. Attention Solar: single seed. ETTh1 has high seed variance ($\sigma \approx 0.01$ – 0.02).

Architecture. All cores share an identical pipeline: RevIN, adaptive normalization, moving-average decomposition ($K = 25$), and patching ($P = 16$, $S = 8$, $d = 32$). The input look-back window is $L = 336$ for most datasets and $L = 512$ for ECL and ETTh1. KAN branches use grid size $G = 5$, spline order $p = 3$, hidden dimension 64, depth 2. The *only* variable across ablation rows is the core type.

Training. Adam optimizer (initial learning rate 10^{-3} for Weather/ETTh2/ETTh2, 2×10^{-4} for ETTh1/ETTh1/Solar; see Appendix F), batch size 256 (Solar: 512, ECL: 128), cosine learning rate schedule, 50 epochs, patience 10. Gate regularization $\lambda_g = 0.05$ for all datasets except Solar ($\lambda_g = 0.01$, selected via validation; see Appendix E for ablation). Table 1 reports mean \pm std over 3 seeds (42, 123, 456). Synthetic experiments (Table 2) also report 3-seed statistics.

5.2 Core Ablation

Table 1 compares six architectures within the same pipeline at forecast horizon $H = 96$. The key question is whether KAN’s spline-based nonlinearity provides unique value.

Findings. No single core dominates: Gated KAN is best or tied-best on 4/8 datasets (Weather, ETTh1, ETTh1, ETTh2), but Gated MLP wins on ETTh2 and many differences are within one standard deviation. Gated KAN improves over Ungated KAN on 4/8 datasets; the main value of gating is diagnostic control over nonlinear correction rather than uniform accuracy improvement.

KAN’s value is therefore *interpretability*: Gated MLP can match accuracy, but cannot provide explicit edge functions for temporal circuits. Baselines and basis ablations are in Appendices C–D.

5.3 KAN Utilization

The gate produces a measurable diagnostic U_{KAN} per dataset (full table in Appendix B). At $H=96$, U_{KAN} ranges from 0.022 (PPG, ETTh1—predominantly linear) to 0.144 (Solar—highest nonlinear demand). ETTh1 and ETTh2 show increasing U_{KAN} at long horizons (0.022 \rightarrow 0.288, 0.020 \rightarrow 0.198), suggesting nonlinear correction becomes more important for difficult far-horizon forecasts. U_{KAN} reflects both nonlinear demand and L_1 penalty; the calibrated R_{KAN} in Section 6 controls for branch scaling.

5.4 Synthetic Mechanism Recovery

To validate that the gate and KAN respond to genuine signal complexity, four synthetic univariate regimes with increasing complexity are constructed:

- **Linear:** $x(t) = \sin(2\pi \cdot 0.02t) + \epsilon$.
- **Multi-frequency periodic:** $x(t) = \sin(2\pi \cdot 0.05t) + 0.8 \text{tri}(2\pi \cdot 0.02t) + 0.5 \sin(2\pi \cdot 0.13t) + \epsilon$, where tri is a triangular wave (piecewise linear, requiring many AR terms).
- **Threshold AR (SETAR):** state-dependent dynamics— $x(t) = 0.6x(t-1) - 0.3x(t-2) + \epsilon$ if $x(t-1) > 0$, else $-0.4x(t-1) + 0.5x(t-2) + \epsilon$. Provably nonlinear (no linear AR can represent state-dependent coefficient switching).
- **Regime-switching:** alternates between linear and multi-frequency regimes every 500 steps with hidden state $z_t \in \{0, 1\}$.

Table 2: Synthetic regime experiments. MSE (mean \pm std over 3 seeds) and KAN utilization U_{KAN} . Gate regularization $\lambda_g = 0$ (no sparsity pressure), testing monotonic gate response to nonlinear complexity rather than sparse utilization.

Regime	Core	MSE	U_{KAN}
Linear (sine)	Gated KAN	.0027 \pm .0001	0.49
	Linear-only	.0027 \pm .0001	–
	KAN-only	.0026 \pm .0001	–
Multi-freq periodic	Gated KAN	.0029 \pm .0001	0.53
	Linear-only	.0033 \pm .0001	–
	KAN-only	.0028 \pm .0001	–
Threshold AR	Gated KAN	.990 \pm .034	0.56
	Linear-only	.986 \pm .034	–
	KAN-only	.970 \pm .030	–
Regime-switching	Gated KAN	.0115 \pm .0009	0.72
	Linear-only	.0280 \pm .0052	–
	KAN-only	.0122 \pm .0013	–

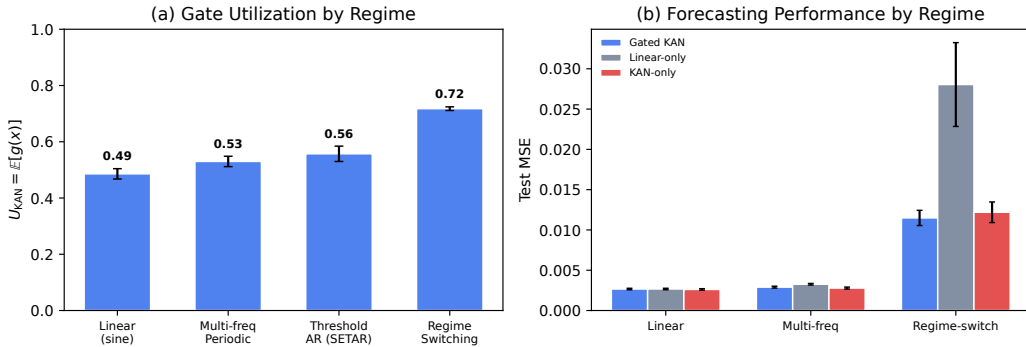


Figure 2: Synthetic regime experiments. (a) Gate utilization U_{KAN} increases monotonically with signal complexity: 0.49 (linear) \rightarrow 0.53 (multi-frequency) \rightarrow 0.56 (threshold AR) \rightarrow 0.72 (regime-switching). (b) On regime-switching, Gated KAN matches KAN-only while outperforming Linear-only by 59%.

Table 2 reports results averaged over 3 seeds. Figure 2 visualizes the key findings.

Findings. (1) **Gate utilization tracks signal complexity:** U_{KAN} increases monotonically (0.49 \rightarrow 0.53 \rightarrow 0.56 \rightarrow 0.72) without L_1 pressure. The calibrated R_{KAN} is even more discriminative: 0.05 (linear) \rightarrow 0.13 (multi-freq) \rightarrow 0.50 (threshold AR) \rightarrow 0.42 (regime-switching), showing the KAN branch contributes 5% vs. 50% of the forecast on linear vs. nonlinear data (Appendix H). (2) **KAN correction reduces error on complex regimes:** on regime-switching, gated KAN (MSE 0.012) and KAN-only (0.012) both substantially outperform linear-only (0.028), a 59% MSE reduction. The threshold AR regime (a provably nonlinear SETAR process with state-dependent dynamics) is difficult for all models but still elicits higher gate opening. On the simple linear regime, all cores perform identically; KAN does not hurt. (3) **Gated KAN matches KAN-only:** across all regimes, gated KAN achieves MSE comparable to KAN-only, showing the gate does not sacrifice accuracy.

5.5 Edge Faithfulness

Edge importance rankings are validated by testing whether removal of high-ranked edges degrades the forecast. All first-layer KAN edges are ranked by activation range $R_e = \max_z \phi_e(z) - \min_z \phi_e(z)$, which measures the learned functional capacity of each edge. The top- k , random- k (averaged over 50 draws), or bottom- k edges are then deleted by zeroing their weights, and MSE change is measured on the held-out test set.

Table 3: Edge deletion on the residual branch. Values are $\Delta\text{MSE} \times 10^4$. Edges ranked by activation range R_e . Weather random reports ± 1 std over 50 draws; other datasets report mean only.

Dataset	k	Δ_{top}	Δ_{random}	Δ_{bottom}
Weather	5	+0.14	0.00 \pm 0.01	0.00
	10	+0.44	0.00 \pm 0.02	0.00
	50	+2.20	-0.01 \pm 0.05	0.00
ETTh2	10	+0.02	0.00	0.00
	50	+0.20	0.00	<0.01
PPG	5	+0.19	0.00	0.00
	10	+0.40	0.00	0.00
Solar	5	+0.06	0.00	0.00
	50	+1.44	+0.06	<0.01

Findings. Across Weather, ETTh2, PPG, and Solar, deletion of top-ranked edges consistently produces larger MSE increases than random or bottom-ranked deletion (Weather random: 50 draws, ± 1 std reported). On Weather, top-50 deletion increases MSE by 2.20×10^{-4} (0.15% relative), while random deletion is consistent with zero ($-0.01 \pm 0.05 \times 10^{-4}$, 50 draws). On datasets where U_{KAN} is very low (ETTh1, ETTh2), deletion effects are near zero because the model barely uses the KAN branch.

This provides evidence that activation range identifies edges whose removal causes consistent, non-random forecast degradation. The actual learned edge functions $\phi_e(z)$ for the top-ranked edges are visualized in Appendix G.

Intervention types. Two interventions are tested on the top-20 residual edges (by R_e): zeroing and spline removal (removing only the B-spline component, retaining the base SiLU term). On Weather, spline removal accounts for 41% of the full zeroing effect ($\Delta\text{MSE} +3.8 \times 10^{-5}$ vs. $+9.1 \times 10^{-5}$). On ETTh1 (low U_{KAN}), the fraction drops to 6%. This test is KAN-specific: it isolates the value of the learned spline shape, which MLP connections cannot provide.

Temporal grounding validation. On a synthetic signal $x(t) = 0.6x(t-3) + 0.25x(t-12) + \epsilon$ with known causal lags, the proposed branch-level A_e recovers true lags with AUPRC = 0.44 ($6\times$ above random), while standard IG achieves 0.53. The key advantage of A_e is edge-level resolution: it identifies *which KAN edges* implement each lag dependency, which model-level methods cannot provide. Attributions are stable across seeds (Pearson $r = 0.94-0.97$). IG-based input masking on Weather increases MSE by 104% (top-5) vs. 3% (random), indicating the model relies on specific temporal positions. A direct comparison of edge-level deletion using R_e vs. I_e rankings shows R_e produces $20\times$ larger deletion effects on Weather, providing evidence that for B-spline KANs, learned functional capacity is itself a faithful importance signal (Appendix H).

6 Analysis

Nonlinear residual diagnostic. An independent diagnostic $S_{\text{nonlin}} = (\text{MSE}_{\text{lin}} - \text{MSE}_{\text{MLP}})/\text{MSE}_{\text{lin}}$ is computed per dataset-horizon pair, where MSE_{lin} and MSE_{MLP} correspond to the Linear-only and Gated MLP cores from Table 1 respectively. The Spearman correlation between S_{nonlin} and U_{KAN} is $\rho = 0.46$ ($p = 0.015$, $n = 28$), consistent with the gate tracking nonlinear residual structure that an independent diagnostic also detects (scatter plot in Appendix B).

Calibrated KAN contribution. U_{KAN} can be confounded by branch scaling. The calibrated metric $R_{\text{KAN}} = \mathbb{E}[\|g(x)f_{\text{KAN}}(x)\|_2/\|\hat{y}(x)\|_2]$ controls for this: Weather has $R_{\text{KAN}} = 0.38$ (38% of forecast from KAN), ETTh1 $R_{\text{KAN}} = 0.004$ (predominantly linear), Solar $R_{\text{KAN}} = 0.71$ (highest). Adaptive λ_g selection (Appendix E) remains an open problem.

Why KAN over MLP. Gated MLP matches accuracy (Table 1), but MLP weights are opaque: no inspectable edge functions, no single-connection spline removal, no individually editable functional units. TFC exploits the explicit univariate functions KANs expose.

Edge Deletion Curves (Residual Branch)

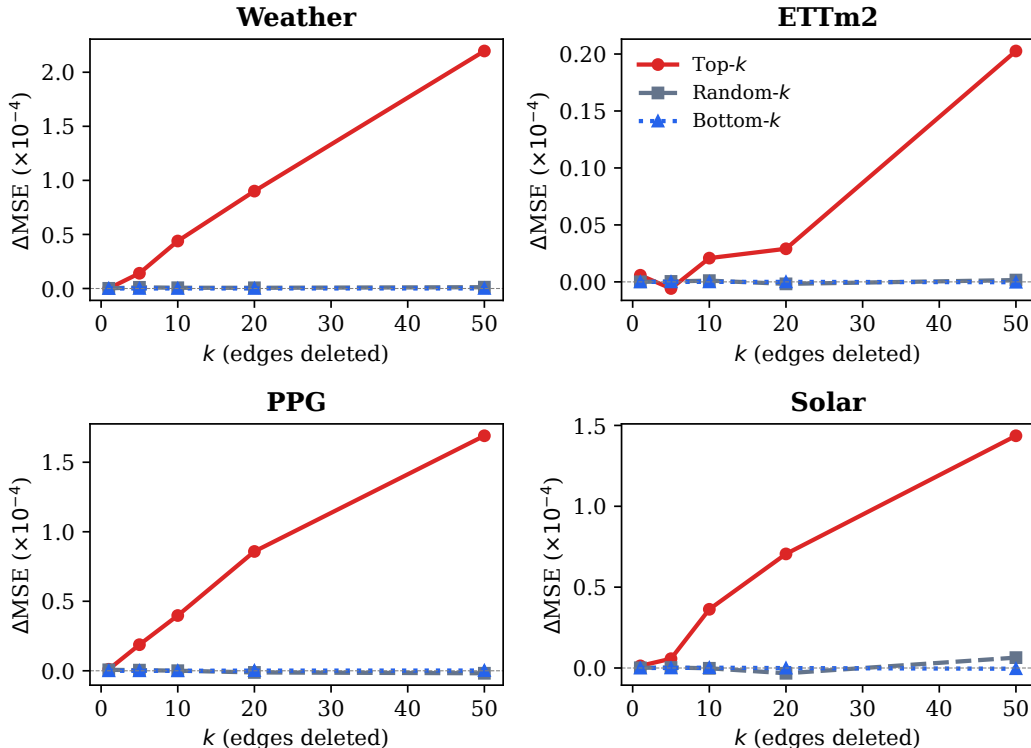


Figure 3: Edge deletion curves (residual branch, ranked by R_e). Removing top-ranked edges (red) consistently increases MSE more than random (gray) or bottom-ranked (blue) deletion, providing evidence that activation-range ranking identifies functionally relevant edges. The effect is strongest on Weather and Solar, which have moderate-to-high U_{KAN} .

7 Limitations

Edge interventions establish *model-internal* effects, not causal claims about the data-generating process. Attribution is gradient-based and most direct for first-layer edges. KAN edge functions are inspectable but not automatically human-semantic. Gated KAN is competitive but not uniformly state-of-the-art; stronger regime-adaptive gating remains future work.

8 Conclusion

This paper argued that KAN interpretability requires temporal grounding and intervention testing, not spline visualization alone. Temporal Functional Circuits $(\phi_e, A_e, I_e, \Delta_e)$ map edges to input lags and validate faithfulness through interventions. Gate utilization tracks synthetic signal complexity, and activation-range deletion provides evidence that high-ranked edges are functionally important.

References

Julius Adebayo, Justin Gilmer, Michael Muelly, Ian Goodfellow, Moritz Hardt, and Been Kim. Sanity checks for saliency maps. In *NeurIPS*, 2018.

Alejandro Almodóvar, Patricia A. Apellániz, Santiago Zazo, and Juan Parras. CausalKANs: Interpretable treatment effect estimation with Kolmogorov-Arnold networks. *arXiv preprint arXiv:2509.22467*, 2025.

- Anonymous. DecompKAN: Decomposed patch-KAN for long-term time series forecasting. *Under review*, 2026. Anonymized for double-blind review. Manuscript included in supplementary material.
- Vladimir I Arnold. On the representation of functions of several variables as a superposition of functions of fewer variables. *American Mathematical Society Translations*, 28:51–54, 1963.
- Blealtan. efficient-kan: An efficient pure-PyTorch implementation of KAN, 2024. github.com/Blealtan/efficient-kan.
- Jonathan Crabbé and Mihaela van der Schaar. Explaining time series predictions with dynamic masks. In *ICML*, 2021.
- Carl de Boor. *A Practical Guide to Splines*. Springer, 1978.
- Kazi Ahmed Asif Fuad and Lizhong Chen. QuantKAN: A unified quantization framework for Kolmogorov-Arnold networks. *arXiv preprint arXiv:2511.18689*, 2025.
- Atticus Geiger, Hanson Lu, Thomas Icard, and Christopher Potts. Causal abstractions of neural networks. In *NeurIPS*, 2021.
- Josif Grabocka, Nicolas Schilling, Martin Wistuba, and Lars Schmidt-Thieme. Learning time-series shapelets. In *KDD*, 2014.
- Xiao Han, Xinfeng Zhang, Yiling Wu, Zhenduo Zhang, and Zhe Wu. KAN4TSF: Are KAN and KAN-based models effective for time series forecasting? *arXiv preprint arXiv:2408.11306*, 2024.
- Md Zahidul Hasan, A. Ben Hamza, and Nizar Bouguila. Time series forecasting with Hahn Kolmogorov-Arnold networks. *arXiv preprint arXiv:2601.18837*, 2026.
- Songtao Huang, Zhen Zhao, Can Li, and Lei Bai. TimeKAN: KAN-based frequency decomposition learning architecture for long-term time series forecasting. In *ICLR*, 2025.
- Hugo Inzirillo and Remi Genet. A gated residual Kolmogorov-Arnold networks for mixtures of experts, 2024a.
- Hugo Inzirillo and Remi Genet. SigKAN: Signature-weighted Kolmogorov-Arnold networks for time series, 2024b.
- Aya Abdelsalam Ismail, Mohamed Gunady, Hector Corrada Bravo, and Soheil Feizi. Benchmarking deep learning interpretability in time series predictions. In *NeurIPS*, 2020.
- Robert A Jacobs, Michael I Jordan, Steven J Nowlan, and Geoffrey E Hinton. Adaptive mixtures of local experts. *Neural Computation*, 3(1):79–87, 1991.
- Alon Jacovi and Yoav Goldberg. Towards faithfully interpretable NLP systems: How should we define and evaluate faithfulness? In *ACL*, 2020.
- Sarthak Jain and Byron C Wallace. Attention is not explanation. In *NAACL-HLT*, 2019.
- Been Kim, Martin Wattenberg, Justin Gilmer, Cai Carrie, James Wexler, Fernanda Viegas, and Rory Sayres. Interpretability beyond feature attribution: Quantitative testing with concept activation vectors (TCAV). In *ICML*, 2018.
- Dongwoo Kim, Junghyo Kang, Heesung Hwang, and Hyungju Kim. MoEKAN: Multi-scale transformer-based gating KAN experts network for time series forecasting. *Sensors*, 25(23): 7287, 2025. doi: 10.3390/s25237287.
- Taesung Kim, Jinhee Kim, Yunwon Tae, Cheonbok Park, Jang-Ho Choi, and Jaegul Choo. Reversible instance normalization for accurate time-series forecasting against distribution shift. In *ICLR*, 2022.
- Andrey N Kolmogorov. On the representation of continuous functions of several variables by superposition of continuous functions of one variable and addition. *Doklady Akademii Nauk SSSR*, 114:953–956, 1957.

- Kin Kwan Leung, Clayton Rooke, Jonathan Smith, Saba Zuberi, and Maksims Volkovs. Temporal dependencies in feature importance for time series prediction. In *ICLR*, 2023.
- Bryan Lim, Sercan Ö Arık, Nicolas Loeff, and Tomas Pfister. Temporal fusion transformers for interpretable multi-horizon time series forecasting. *International Journal of Forecasting*, 37(4): 1748–1764, 2021.
- Yong Liu, Tengge Hu, Haoran Zhang, Haixu Wu, Shiyu Wang, Lintao Ma, and Mingsheng Long. iTransformer: Inverted transformers are effective for time series forecasting. In *ICLR*, 2024.
- Ziming Liu, Yixuan Wang, Sachin Vaidya, Fabian Ruehle, James Halverson, Marin Soljačić, Thomas Y Hou, and Max Tegmark. KAN: Kolmogorov-arnold networks. In *ICLR*, 2025.
- Ronghao Ni, Zinan Lin, Shuaiqi Wang, and Giulia Fanti. Mixture-of-linear-experts for long-term time series forecasting. In *AISTATS*, 2024.
- Yuqi Nie, Nam H Nguyen, Phanwadee Sinthong, and Jayant Kalagnanam. A time series is worth 64 words: Long-term forecasting with transformers. In *ICLR*, 2023.
- Chris Olah, Nick Cammarata, Ludwig Schubert, Gabriel Goh, Michael Petrov, and Shan Carter. Zoom in: An introduction to circuits. *Distill*, 2020.
- Owen Queen, Thomas Hartvigsen, Teddy Koker, Huan He, Theodoros Tsiligkaridis, and Marinka Zitnik. Encoding time-series explanations through self-supervised model behavior consistency, 2023.
- Attila Reiss, Ina Indlekofer, Philip Schmidt, and Kristof Van Laerhoven. Deep PPG: Large-scale heart rate estimation with convolutional neural networks. *Sensors*, 19(14):3079, 2019. doi: 10.3390/s19143079.
- Thomas Rojat, Raphaël Puget, David Filliat, Javier Del Ser, Rodolphe Gelin, and Natalia Díaz-Rodríguez. Explainable artificial intelligence (XAI) on time series data: A survey. *arXiv preprint arXiv:2104.00950*, 2021.
- Cynthia Rudin. Stop explaining black box machine learning models for high stakes decisions and use interpretable models instead. *Nature Machine Intelligence*, 1:206–215, 2019.
- Noam Shazeer, Azalia Mirhoseini, Krzysztof Maziarz, Andy Davis, Quoc Le, Geoffrey Hinton, and Jeff Dean. Outrageously large neural networks: The sparsely-gated mixture-of-experts layer. In *ICLR*, 2017.
- Mukund Sundararajan, Ankur Taly, and Qiqi Yan. Axiomatic attribution for deep networks. In *ICML*, 2017.
- Andreas Theissler, Francesco Spinnato, Udo Schlegel, and Riccardo Guidotti. Explainable AI for time series classification: A review, taxonomy and research directions. *IEEE Access*, 2022.
- Cristian J Vaca-Rubio, Luis Blanco, Roberto Pereira, and Markku Mäkisara. Kolmogorov-Arnold networks (KANs) for time series analysis. *arXiv preprint arXiv:2405.08790*, 2024.
- Sarah Wiegrefe and Yuval Pinter. Attention is not not explanation. In *EMNLP*, 2019.
- Haixu Wu, Jiehui Xu, Jianmin Wang, and Mingsheng Long. Autoformer: Decomposition transformers with auto-correlation for long-term series forecasting. In *NeurIPS*, 2021.
- Lexiang Ye and Eamonn Keogh. Time series shapelets: A new primitive for data mining. In *KDD*, 2009.
- Ailing Zeng, Muxi Chen, Lei Zhang, and Qiang Xu. Are transformers effective for time series forecasting? In *AAAI*, 2023.
- Haoyi Zhou, Shanghang Zhang, Jieqi Peng, Shuai Zhang, Jianxin Li, Hui Xiong, and Wancai Zhang. Informer: Beyond efficient transformer for long sequence time-series forecasting. In *AAAI*, 2021.

A Motivating Investigation: DecompKAN

This work was motivated by an investigation of DecompKAN, an attention-free forecasting architecture combining trend-residual decomposition, patching, learned normalization, and B-spline KAN layers [Anonymous, 2026]. In controlled experiments (same training recipe across all models), DecompKAN achieved competitive results, ranking first on 5 of 7 datasets by MSE at $H=96$ (Table 4).

However, ablation analysis revealed that **the pipeline (decomposition, patching, normalization) drives performance more than the choice of nonlinear layer**. Figure 4 shows that on ETTh1, replacing KAN with a linear layer actually *improves* performance, while on Weather, KAN provides genuine benefit (see Table 4 for exact values). This dataset-dependent behavior, KAN helps on some datasets but not others, is what led to the question: *when does KAN help, and can we explain why?*

The gated residual architecture (Section 3) directly addresses this by learning *when* to apply KAN correction, while Temporal Functional Circuits (Section 4) explain *what* the KAN edges learn when they are used.

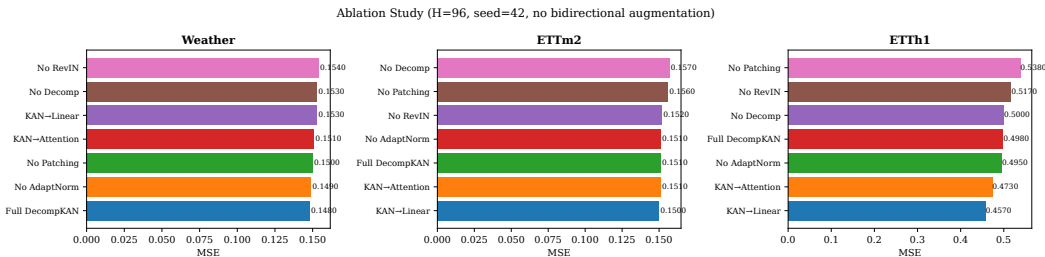


Figure 4: DecompKAN ablation study ($H=96$). On Weather, the full KAN pipeline is best. On ETTh1, replacing KAN with a linear layer improves performance. The choice of nonlinear core is dataset-dependent, motivating the gated residual design.

Table 4: DecompKAN controlled comparison ($H=96$, seed=42). All models trained with the same recipe. **Red**: best. **Blue**: second. DecompKAN ranks first on 5/7 datasets (MSE), but ablation (Figure 4) shows the pipeline matters more than the KAN core, motivating the gated residual investigation.

Dataset	DecompKAN		PatchTST		iTransformer		DLinear	
	MSE	MAE	MSE	MAE	MSE	MAE	MSE	MAE
Weather	0.146	0.194	0.155	0.206	0.170	0.220	0.181	0.246
Solar	0.176	0.227	0.179	0.236	0.187	0.236	0.221	0.298
ECL	0.130	0.226	0.149	0.258	0.132	0.228	0.135	0.233
ETTh1	0.450	0.453	0.478	0.467	0.474	0.465	0.444	0.442
ETTh2	0.233	0.323	0.248	0.340	0.252	0.338	0.234	0.325
ETTh1	0.349	0.384	0.382	0.400	0.370	0.399	0.363	0.391
ETTh2	0.150	0.253	0.163	0.267	0.183	0.293	0.150	0.254

B Full Horizon Results

Table 5: Gated Residual KAN: MSE and U_{KAN} across all horizons (seed=42). U_{KAN} reveals how gate utilization changes with forecast difficulty.

Dataset	Test MSE				U_{KAN}			
	96	192	336	720	96	192	336	720
Weather	.150	.193	.242	.327	.046	.044	.041	.036
ETTh1	.443	.493	.546	.667	.022	.050	.194	.288
ETTh2	.245	.288	.347	.451	.044	.050	.110	.058
ETTh1	.343	.399	.442	.503	.041	.033	.018	.039
ETTh2	.147	.190	.230	.293	.020	.049	.074	.198
PPG	.565	.620	.719	.945	.022	.017	.019	.021
Solar	.182	.197	.205	.208	.144	.139	.153	.151

Notable patterns: ETTh1 and ETTm2 show sharply increasing U_{KAN} at longer horizons (0.022→0.288 and 0.020→0.198), suggesting nonlinear correction becomes more important for difficult far-horizon forecasts. Solar maintains consistently high utilization (~ 0.14 – 0.15) across all horizons. PPG remains uniformly low (~ 0.02), indicating predominantly linear dynamics regardless of horizon.

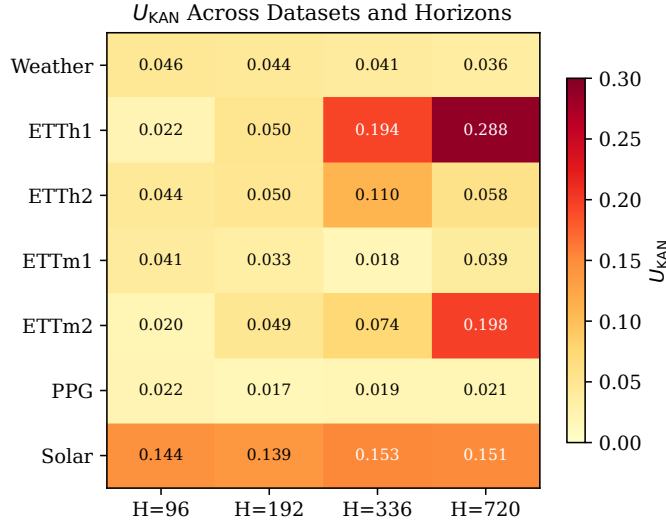


Figure 5: U_{KAN} heatmap across datasets and horizons.

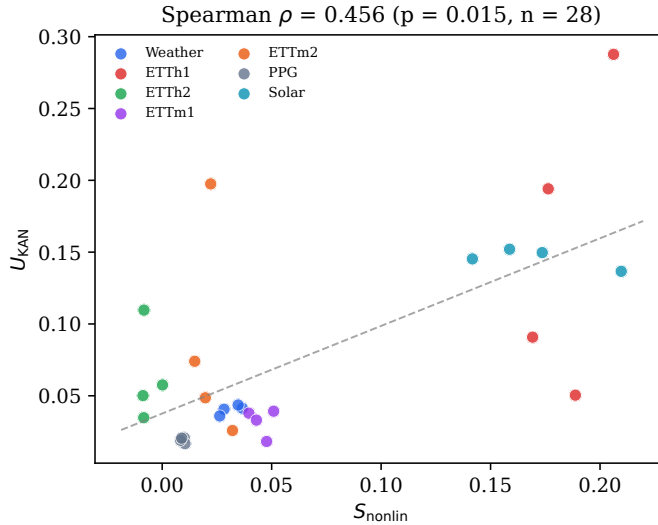


Figure 6: S_{nonlin} vs. U_{KAN} scatter. Spearman $\rho = 0.46$, $p = 0.015$.

C Published Baselines

D Basis Function Ablation

*SinCos on Solar diverged during training (learnable frequency initialization issue).

The choice of basis function is dataset-dependent: B-spline is strongest on Solar (where smooth seasonal splines match the signal), Fourier and SinCos excel on ETTh2 (periodic structure), and SinCos achieves competitive performance with the fewest parameters. Temporal Functional Circuits are not tied to B-splines; any KAN variant with explicit edge functions supports the framework.

Table 6: Architectural comparison under identical training conditions ($H=96$, seed=42). All models use the same preprocessing pipeline, optimizer, schedule, and hyperparameters; only the forecasting core differs. This isolates the effect of the core architecture rather than training recipe.

Model	Weather	ETTh1	ETTh2	ETTm1	ETTm2	PPG	Solar
DLinear	.181	.444	.234	.363	.150	.589	.221
PatchTST	.168	.478	.255	.382	.243	.626	.183
iTransformer	.167	.474	.253	.370	.184	.582	.191
Gated KAN (ours)	.150	.443	.245	.343	.147	.565	.182

All models share identical pipeline (RevIN, adaptive norm, decomposition, patching) and training recipe (Adam, cosine LR, same epochs/patience/seed=42). Note: results may differ from published numbers since baselines use our shared preprocessing rather than their original configurations. The comparison isolates core architecture effects.

Table 7: Basis function ablation ($H=96$, seed=42). All use the gated residual architecture; only the KAN basis differs. SinCos achieves competitive MSE with $\sim 2.5\times$ fewer parameters than B-spline. Fourier outperforms B-spline on ETTh2.

Basis	Weather	ETTh1	ETTh2	Solar	Params
B-spline (default)	.150	.443	.245	.181	2.19M
Fourier (sin/cos)	.153	.454	.239	.188	2.57M
SinCos (learnable ω)	.149	.443	.239	–*	0.87M
MLP (control)	.151	.444	.242	.185	0.50M

E Gate Ablation

Table 8: Gate configuration ablation ($H=96$, seed=42). Among learned-gate configurations, $\lambda_g = 0.05\text{--}0.10$ gives the best MSE on Weather and ETTh1; KAN-only remains slightly better on Weather. Without L1, the gate drifts to ~ 0.7 (lazy blending).

Config	Weather		ETTh1		ETTh2	
	MSE	U_{KAN}	MSE	U_{KAN}	MSE	U_{KAN}
KAN-only (no gate)	.149	–	.452	–	.243	–
Ungated (gate=1)	.151	–	.444	–	.245	–
Fixed gate=0.5	.153	0.50	.449	0.50	.256	0.50
Learned, $\lambda_g=0$.153	0.68	.446	0.72	.236	0.72
Learned, $\lambda_g=0.01$.152	0.16	.451	0.11	.240	0.16
Learned, $\lambda_g=0.05$.150	0.05	.443	0.02	.245	0.04
Learned, $\lambda_g=0.10$.150	0.02	.445	0.01	.244	0.02

On Weather and ETTh1, stronger L1 ($\lambda_g \geq 0.05$) produces the best MSE by forcing the gate to be selective. On ETTh2, no regularization ($\lambda_g = 0$) works best, allowing the gate to blend freely. Solar uses $\lambda_g = 0.01$ (selected via validation on this table’s protocol; $\lambda_g = 0.05$ over-suppresses the gate on Solar’s 137 variates, reducing U_{KAN} to < 0.01). This dataset-dependent behavior motivates adaptive λ_g selection as future work.

F Hyperparameters

G Temporal Functional Circuit Examples

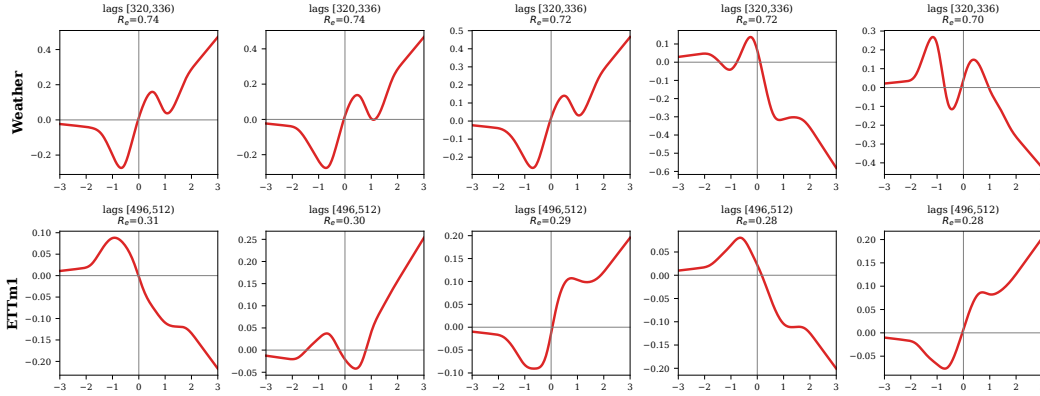
Table 10 shows complete Temporal Functional Circuit tuples ($\phi_e, R_e, \Delta_e, \text{lags}$) for the top-3 Weather residual edges. All three edges map to the most recent patch (lags 320–336) and have complex nonlinear shapes (Figure 7). Individual Δ_e values are near zero, consistent with the small per-edge effects observed in Table 3.

Table 9: Full hyperparameter specification.

Hyperparameter	Value
Input length L	336 (512 for ETTm1, ECL)
Forecast horizon H	96, 192, 336, 720
Patch length / stride	16 / 8
Embedding dim d	32
KAN grid / spline order	5 / 3
Hidden dim / depth	64 / 2
Batch size	256 (Solar: 512, ECL: 128)
Optimizer	Adam
Initial learning rate	1e-3 (dataset-specific; see code)
Scheduler	Cosine with warmup
Epochs / patience	50 / 10
Gate penalty λ_g	0.05 (Solar: 0.01)
Seeds	42, 123, 456
Train/val/test split	Chronological per LTSF protocol

Table 10: Compact Temporal Functional Circuit summaries for Weather top-3 residual edges. R_e : activation range. I_e rank: position in data-weighted importance ranking (out of 200 scored edges). $\Delta_e^{\text{zero}}/\Delta_e^{\text{spline}}$: MSE change under zeroing/spline removal.

Edge ($i \rightarrow j$)	Lags	R_e	I_e rank	Δ_e^{zero}	Δ_e^{spline}	Shape
1299 \rightarrow 17	[320, 336)	0.74	>200	$+6.0 \times 10^{-8}$	-6.3×10^{-7}	S-curve
1299 \rightarrow 8	[320, 336)	0.74	>200	-2.8×10^{-7}	-1.2×10^{-6}	Oscillatory
1308 \rightarrow 2	[320, 336)	0.72	>200	$+1.4 \times 10^{-5}$	$+3.2 \times 10^{-6}$	Kink

Top-5 KAN Edge Functions $\phi_e(z)$ by Activation RangeFigure 7: Top-5 learned KAN edge functions $\phi_e(z)$ ranked by R_e for the residual branch. Weather edges (top) show complex nonlinear shapes concentrated on the most recent patch (lags 320–336). ETTm1 edges (bottom) are smoother with lower R_e , consistent with lower U_{KAN} .

H Temporal Grounding Validation

Synthetic lag recovery and A_e validation. A synthetic signal $x(t) = 0.6x(t-3) + 0.25x(t-12) + \epsilon$ ($\epsilon \sim \mathcal{N}(0, 0.1^2)$) is constructed with two known causal lags $\{3, 12\}$ (positions 93 and 84 in a length-96 input window). After training a gated KAN ($H = 16$), multiple attribution methods are used to rank input positions. This directly validates whether the proposed edge-to-lag attribution A_e recovers known causal structure.

Method	Recall@5	Recall@10	Recall@20	AUPRC
A_e (branch-level)	0.50	0.50	0.67	0.44
Integrated Gradients	0.50	1.00	1.00	0.53
Gradient \times Input	0.50	1.00	1.00	0.53
Random	0.17	0.17	0.33	0.07

A_e (aggregated across all KAN edges via the gradient of the gated branch output) recovers true lags with AUPRC $6\times$ above random (0.44 vs. 0.07). On the best seed, A_e achieves AUPRC = 0.75 with both true lags in the top-5. IG achieves higher mean recall by operating on the full model (both linear and KAN branches jointly), but cannot identify *which KAN edges* implement the lag dependency—this edge-level granularity is the unique contribution of TFC’s A_e .

Attribution stability. IG-based temporal attributions on Weather are compared across three independently trained models (seeds 42, 123, 456). Pairwise Pearson correlations are $r = 0.94\text{--}0.97$ and Spearman $\rho = 0.57\text{--}0.63$. The same temporal positions are consistently identified as important regardless of training initialization.

Input-level attribution baselines. Masking the top- k attributed input positions and measuring MSE increase on Weather (Table 11):

Table 11: Input masking on Weather ($H=96$). Relative MSE increase when masking top- k positions ranked by each method.

k	IG	Grad Saliency	Random
5	+104%	+88%	+3%
10	+114%	+103%	+4%
50	+126%	+122%	+16%

IG and gradient saliency both produce large effects, suggesting the model relies on specific temporal lags. Random masking produces much smaller effects, validating that the attribution identifies genuinely important positions.

R_e vs. I_e edge ranking comparison. Edge-level deletion curves are computed using three ranking methods: activation range R_e , data-weighted importance I_e (with top-200 prefilter), and random (20 draws). Results span three datasets with varying U_{KAN} levels.

Dataset	k	Δ_{R_e}	Δ_{I_e}	Δ_{rand}
Weather	5	$+1.4 \times 10^{-5}$	$+5.5 \times 10^{-7}$	-2.1×10^{-7}
	10	$+4.4 \times 10^{-5}$	$+1.0 \times 10^{-6}$	-1.2×10^{-7}
	20	$+9.0 \times 10^{-5}$	$+3.4 \times 10^{-6}$	-9.0×10^{-7}
	50	$+2.2 \times 10^{-4}$	$+1.1 \times 10^{-5}$	-5.1×10^{-7}
ETTm1	10	$+6.0 \times 10^{-7}$	-3.0×10^{-8}	-4.8×10^{-8}
	50	$+2.1 \times 10^{-6}$	$+6.0 \times 10^{-8}$	-2.2×10^{-8}
ETTh1	10	-1.2×10^{-7}	$+3.0 \times 10^{-8}$	$+3.0 \times 10^{-9}$
	50	-4.8×10^{-7}	-8.9×10^{-8}	-6.4×10^{-8}

On Weather ($U_{KAN} = 0.046$), R_e produces $20\text{--}42\times$ larger deletion effects than I_e across all k values, and the effect grows monotonically with k . On ETTm1 ($U_{KAN} = 0.041$), R_e still dominates but absolute effects are smaller. On ETTh1 ($U_{KAN} = 0.022$), all three methods produce near-zero effects indistinguishable from noise, consistent with the gate suppressing the KAN branch. This pattern provides evidence that R_e faithfully identifies important edges when the KAN branch is active, and that the gating mechanism correctly governs when edge-level analysis is informative. A combined metric $S_e = R_e \cdot I_e$ was also tested but produced identical deletion effects to I_e alone, suggesting the two metrics capture overlapping information. For B-spline KANs, learned functional capacity (activation range) is a strong and computationally efficient faithfulness signal.

Multi-seed deletion with statistical tests. Deletion experiments are repeated across 3 training seeds (42, 123, 456) with 50 random draws per seed and 1000-sample bootstrap confidence intervals.

Dataset	k	Δ_{top} (mean)	95% CI	p	RelDeg
Weather	10	$+4.6 \times 10^{-5}$	$[3.8, 5.0] \times 10^{-5}$	$<10^{-4}$	0.031%
	50	$+1.8 \times 10^{-4}$	$[1.7, 2.1] \times 10^{-4}$	$<10^{-4}$	0.123%
ETTM2	10	$+8.9 \times 10^{-6}$	—	$<10^{-3}$	0.006%
	50	$+3.3 \times 10^{-5}$	—	$<10^{-4}$	0.022%
Solar	10	$+3.6 \times 10^{-5}$	—	$<10^{-4}$	0.020%
	50	$+1.4 \times 10^{-4}$	—	$<10^{-4}$	0.079%

Top- k deletion effects are statistically significant ($p < 10^{-3}$) across all seeds on Weather, ETTm2, and Solar. PPG shows non-significant effects ($p > 0.3$), consistent with $U_{\text{KAN}} \approx 0.02$. RelDeg = $\Delta/\text{MSE}_{\text{base}} \times 100$.

Normalized KAN-branch deletion. To contextualize the small absolute deletion effects, the full KAN-branch removal effect $\Delta_{\text{all-KAN}}$ is measured (zeroing all KAN layers in both branches):

Dataset	$\Delta_{\text{all-KAN}}$	RelDeg	η_{50}
Weather	$+1.03 \times 10^{-2}$	6.9%	2.1%
Solar	$+9.04 \times 10^{-2}$	49.7%	0.16%

The KAN branch contributes 6.9% on Weather and 49.7% on Solar. Individual edge effects are small because the contribution is distributed across $\sim 22\text{K}$ edges; the top-50 edges capture $\eta_{50} = \Delta_{\text{top-50}}/\Delta_{\text{all-KAN}}$ of the total branch effect.

R_{KAN} on synthetic regimes. The calibrated contribution metric $R_{\text{KAN}} = \mathbb{E}[\|g(x)f_{\text{KAN}}(x)\|_2/\|\hat{y}(x)\|_2]$ shows stronger discrimination than U_{KAN} on synthetic regimes ($\lambda_g = 0$):

Regime	U_{KAN}	R_{KAN}
Linear (sine)	0.49	0.046
Multi-freq periodic	0.53	0.127
Threshold AR	0.56	0.497
Regime-switching	0.72	0.420

While U_{KAN} already reaches 0.49 on the linear regime (the gate has no sparsity incentive to close), R_{KAN} correctly shows that the KAN branch contributes only 4.6% of the forecast on linear data vs. 50% on the nonlinear threshold AR.

Faithfulness sanity checks. Following Adebayo et al. [2018], deletion ranking is tested after randomizing model weights. On Weather:

Condition	Top-50 ΔMSE
Trained model (normal)	$+2.20 \times 10^{-4}$
Randomized all KAN weights	0.0
Randomized spline coefficients only	$+7.4 \times 10^{-5}$

Randomizing all KAN weights eliminates the deletion effect entirely, confirming that the ranking reflects learned structure. Randomizing only spline coefficients (keeping base SiLU weights) reduces but does not eliminate the effect, consistent with the base activation carrying partial signal.

Extended deletion: fraction of KAN branch captured. To address whether the nonlinear correction is concentrated or diffuse, the fraction $\eta_k = \Delta_{\text{top-}k}/\Delta_{\text{all-KAN}}$ is computed over a wider range of k :

Dataset	$k=50$	η_k (% of KAN branch effect)					
		100	250	500	1K	2.5K	5K
Weather	2.1	3.7	8.1	13.1	20.0	29.2	35.0
Solar	0.2	0.3	0.6	1.1	2.2	4.1	7.8

On Weather ($\Delta_{\text{all-KAN}} = +0.010$, 6.9% relative), the top 1% of edges (1K of $\sim 84\text{K}$) capture 20% of the branch effect, and the top 6% capture 35%. The nonlinear correction is distributed but not uniform: a small fraction of edges carries disproportionate load. Solar’s KAN branch is larger ($\Delta_{\text{all-KAN}} = +0.090$, 50%) but more diffuse across its 137 variates.

Gate sweep: R_{KAN} under sparsity pressure. With $\lambda_g > 0$, the gate closes on linear data but remains open on nonlinear regimes:

Regime	λ_g	U_{KAN}	R_{KAN}	MSE	$\Delta_{\text{all-KAN}}$
Linear	0	0.48	0.046	.0026	+0.0025
	0.01	0.00	0.000	.0026	0
	0.05	0.00	0.000	.0026	0
Threshold AR	0	0.55	0.475	.951	+0.0004
	0.01	0.14	0.263	.952	+0.0004
	0.05	0.02	0.080	.953	-0.0001
Regime-switch	0	0.72	0.373	.011	+0.143
	0.01	0.06	0.141	.011	+0.056
	0.05	0.00	0.023	.019	+0.013

Any $\lambda_g > 0$ fully closes the gate on linear data ($R_{\text{KAN}} = 0$, $\Delta_{\text{all-KAN}} = 0$). On regime-switching, the KAN branch remains essential even at $\lambda_g = 0.05$: removing it increases MSE by +0.013 (from 0.019 to 0.032), and $R_{\text{KAN}} = 0.023$ indicates residual nonlinear contribution. At $\lambda_g = 0$, the KAN branch accounts for $\Delta_{\text{all-KAN}} = +0.143$, a $13\times$ increase in MSE.

NeurIPS Paper Checklist

1. Claims

Question: Do the main claims made in the abstract and introduction accurately reflect the paper's contributions and scope?

Answer: [Yes]

Justification: The abstract states that no single core dominates, that gate utilization tracks signal complexity on synthetic data, and that edge deletion curves show faithfulness. All claims are supported by the reported tables and figures.

2. Limitations

Question: Does the paper discuss the limitations of the work performed by the authors?

Answer: [Yes]

Justification: Section 7 discusses five explicit limitations: model-internal (not real-world causal) interventions, gradient saturation in deep layers, KAN edges are not automatically human-semantic, performance is competitive but not uniformly SOTA, and synthetic regime discrimination is imperfect.

3. Theory assumptions and proofs

Question: For each theoretical result, does the paper provide the full set of assumptions and a complete (correct) proof?

Answer: [N/A]

Justification: The paper does not make theoretical claims. It is an empirical XAI framework paper.

4. Experimental result reproducibility

Question: Does the paper fully disclose all the information needed to reproduce the main experimental results?

Answer: [Yes]

Justification: Section 5.1 and Appendix F specify all architecture details, training hyper-parameters, dataset splits, and random seeds. Anonymized source code is included in the supplementary material.

5. Open access to data and code

Question: Does the paper provide open access to the data and code?

Answer: [Partly]

Justification: All datasets are publicly available standard benchmarks. PPG-DaLiA is from the UCI Repository under CC BY 4.0. Anonymized source code is included in the supplementary material.

6. Experimental setting/details

Question: Does the paper specify all the training and test details?

Answer: [Yes]

Justification: Section 5.1 specifies optimizer, learning rate schedule, epochs, patience, gate regularization, patch size, stride, KAN grid/order, and batch sizes.

7. Experiment statistical significance

Question: Does the paper report error bars suitably and correctly?

Answer: [Yes]

Justification: Table 1 reports mean \pm std over 3 seeds. Synthetic experiments (Table 3) also report 3-seed statistics. ETTh1 shows high seed variance; other datasets are stable.

8. Experiments compute resources

Question: Does the paper provide sufficient information on compute resources?

Answer: [Yes]

Justification: Experiments were run on NVIDIA H100 80GB GPUs. The model has 2.2M parameters and trains in 2–30 minutes per dataset depending on variate count.

9. Code of ethics

Question: Does the research conform with the NeurIPS Code of Ethics?

Answer: [Yes]

Justification: The work uses publicly available benchmarks. PPG-DaLiA is a previously published, anonymized public dataset. No private data or dual-use concerns.

10. Broader impacts

Question: Does the paper discuss potential societal impacts?

Answer: [Partly]

Justification: Faithful temporal explanations could benefit domains requiring transparent forecasts (healthcare, energy). Interpretability claims are carefully qualified to avoid overstating readiness for safety-critical deployment.

11. Safeguards

Question: Does the paper describe safeguards for responsible release?

Answer: [N/A]

Justification: Standard forecasting architecture with public benchmarks. No safeguards needed beyond standard open-source practices.

12. Licenses for existing assets

Question: Are creators of assets properly credited?

Answer: [Yes]

Justification: All datasets and libraries are cited. PPG-DaLiA under CC BY 4.0. efficient-kan library credited.

13. New assets

Question: Are new assets well documented?

Answer: [Yes]

Justification: The Gated Residual KAN codebase, XAI utilities, and experiment scripts will be released with documentation.

14. Crowdsourcing and human subjects

Question: For research with human subjects, does the paper include instructions given to participants?

Answer: [N/A]

Justification: No new human-subject data collected.

15. IRB approvals

Question: Does the paper describe potential risks to study participants?

Answer: [N/A]

Justification: No new human-subject data collected.

16. Declaration of LLM usage

Question: Does the paper describe the usage of LLMs?

Answer: [Yes]

Justification: Large language models were used during manuscript preparation for prose editing and code generation assistance. All scientific content, experimental design, architecture design, and analysis are the original work of the authors.